JOURNAL OF SPACECRAFT AND ROCKETS
Vol. 33, No. 2, March–April 1996

Cone-Derived Waverider Flowfield Simulation Including Turbulence and Off-Design Conditions

Yijian Shi,* Bor-Jang Tsai,* and John B. Miles†
University of Missouri–Columbia, Columbia, Missouri 65211
and
Kakkattukuzhy M. Isaac‡
University of Missouri–Rolla, Rolla, Missouri 65401

Using the numerical scheme of Roe's flux-difference splitting, the Baldwin–Lomax algebraic turbulent model, and the time-averaged thin-layer Navier–Stokes equation, the flowfields for a selected Rasmussen's waverider forebody are investigated. Specific cases include turbulent flow on-design condition ($M_\infty = 4$, $\alpha = 0$), turbulent flow off-design condition ($M_\infty = 4$, $\alpha = 5$ deg), and laminar (and Euler) flow off-design condition ($M_\infty = 5$, $\alpha = 0$). For comparison purposes, some results previously reported by the authors are presented. The off-design flowfields are more complicated than the on-design ones. For the $M_\infty = 5$ waverider, there is very strong stock-wave/boundary-layer interaction. For the $\alpha = 5$ deg waverider, there is a detached shock, resulting in a small separation bubble and a vortex on the upper surface. The shock-wave/boundary-layer interaction and shock attachment pattern strongly affect the waverider pressure and local skin-friction coefficient distributions.

Nomenclature

A_b = waverider forebody base area, m^2
C_D = waverider forebody drag coefficient (with $p_b = p_\infty$), (drag)/$\frac{1}{2}\rho_\infty U_\infty^2 A_b$
C_f = local skin-friction coefficient, $\tau/\frac{1}{2}\rho_\infty U_\infty^2$
C_L = waverider forebody lift coefficient normal to freestream, (lift)/$\frac{1}{2}\rho_\infty U_\infty^2 A_b$
C_p = pressure coefficient, $(p - p_\infty)/\frac{1}{2}\rho_\infty U_\infty^2$
F, G, H = inviscid flux terms
H_v = viscous flux term
L = characteristic length, m
M = Mach number
n = normal distance, m
p = pressure, Pa
p_b = waverider forebody base pressure, Pa
Q = conserved variable vector in generalized coordinates
Re = Reynolds number
T = temperature, °R
t = time variable, s
U = freestream velocity, m/s
u, v, w = velocity components in x_i, m/s
x_i = Cartesian coordinates $[x, y, z]^t$
x^i = generalized coordinates $[\xi, \eta, \zeta]^t$
α = angle of attack, deg
μ = total viscosity, kg/m-s
μ_l = laminar viscosity, kg/m-s
μ_t = turbulent eddy viscosity, kg/m-s
ρ = density, kg/m^3
τ = shear stress, $(\mu_l + \mu_t)[d\sqrt{(u^2 + v^2 + w^2)}/dn]$, Pa

Subscripts

∞ = freestream
0 = boundary-layer edge

Received Aug. 1, 1994; revision received June 5, 1995; accepted for publication June 6, 1995.

*Graduate Research Assistant, Department of Mechanical and Aerospace Engineering. Student Member AIAA.
†Professor, Department of Mechanical and Aerospace Engineering. Senior Member AIAA.
‡Associate Professor, Department of Mechanical and Aerospace Engineering and Engineering Mechanics. Member AIAA.

Introduction

TO design a hypersonic flight vehicle, the most difficult problem in aerodynamics is to overcome the tremendous drag and to gain as much lift as possible (or how to obtain a higher lift-to-drag ratio in high supersonic flight). A prospective configuration to satisfy this requirement is the waverider that is designed to efficiently use the high pressure of the flowfield on the lower surface resulting from the strong oblique shock that is attached at the leading edges.

Waveriders have evolved from early re-entry vehicle design. Based on two-dimensional supersonic flows, some early waverider configurations with a caret shape have been derived.[1,2] Recently by using the stream surface associated with the axisymmetric flow past a cone, some new waverider configurations with curved surfaces have been presented.[3–6] In this paper, the authors have chosen Rasmussen's waverider forebody configurations[4] as a model for investigating the waverider flowfield. This configuration (Fig. 1) is relatively simple, and its lower surface can be expressed by a closed mathematical formula. The lower surface is a stream surface that is generated by analyzing inviscid flow past an elliptic cone, whereas the upper surfaces are flat plates. There are several desirable aerodynamic properties about this configuration such as a high lift-to-drag ratio because of high pressure on the lower surface and a relatively uniform flowfield near the centerline on the lower surface. The latter feature is very important for a scramjet integration design.[7,8] Also, this waverider configuration satisfies the more demanding internal volume requirement of waveriders. In addition, some useful experimental results for this configuration have already been obtained[9,10] and are available for comparison purposes. Computational fluid

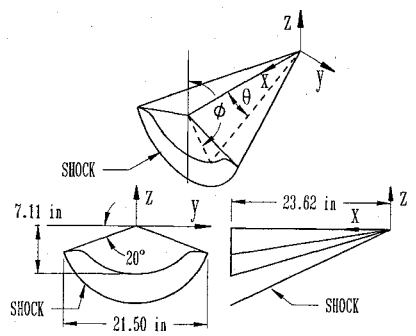

Fig. 1 Geometry of the conical waverider: $\theta = 18.62\{1 - 0.1\cos 2\phi + (0.39 + 0.1\cos 2\phi)[\tan(\pi - \phi)/2.75]^{7.69}\}$ deg.

dynamics[11] for solving the Euler equations have been employed to the same waverider, yielding some interesting comparative results. However, the inviscid assumption will result in incorrect simulations of the flowfield near the waverider surface, the most obvious shortcoming being the omission of friction drag and aerodynamic heating, especially near the waverider tip where there are very strong viscous effects and pressure gradients. In addition, viscosity causes boundary-layer growth that displaces the flowfield from the physical boundaries of the vehicle. This displacement effect does have some influence on the performance of waveriders, especially at high altitude (i.e., low Reynolds number). When the boundary-layer displacement is large, the shock-wave geometry differs from its design condition and, as a result, the pressure distributions are also perturbed. Moreover, during vehicle maneuvering or off-design conditions, such viscous-impacted phenomena as shock-wave/boundary-layer interactions, leading-edge flows, wake flows, and other flows that involve strong viscous-inviscid interactions resulting in large separated flow regions might occur. Obviously, it is not possible to obtain complete and accurate information on the flowfield using the simplified inviscid flow equations.

Progress at simulating viscous waverider flowfields has been previously made and reported,[12,13] using the computer code entitled CFL3D. Laminar and turbulent on-design ($M_\infty = 4$, $\alpha = 0$) supersonic flowfields, associated with the forebody of conical waveriders, were analyzed.

A flight vehicle cannot always stay on its on-design condition because of maneuvering flight. Thus the waverider flowfield research on off-design conditions is very important. The present study will investigate off-design flowfields about the forebody of the same conical waverider. Turbulent off-design ($\alpha = 5$ deg) and laminar off-design ($M_\infty = 5$) cases are simulated in this numerical study. In addition, the authors' earlier on-design results are briefly reviewed and used to compare with the off-design simulations. For additional off-design computations of a viscous optimized waverider, see Ref. 14.

Governing Equations and Numerical Algorithm

The thin-layer Navier–Stokes governing equations[15] to be satisfied are given by Eq. (1), written in generalized coordinates and conservative form. The generalized coordinates $x^i = [\xi, \eta, \zeta]^t$ in the equation are with respect to the Cartesian variables $x_i = [x, y, z]^t$. A calorically perfect gas was assumed. The viscosity μ is described by Sutherland's law as a function of temperature:

$$\frac{\partial}{\partial t}(Q) + \frac{\partial}{\partial \xi}(F) + \frac{\partial}{\partial \eta}(G) + \frac{\partial}{\partial \zeta}(H - H_v) = 0 \qquad (1)$$

To solve Eq. (1), the approximate Riemann solver of Roe[16] is used for the numerical representation of the inviscid fluxes. The quantity Q in the inviscid fluxes is obtained by using the MUSCL (monotone upstream-centered schemes for conservation laws) interpolation of the primitive variables ρ, u, v, w, and p. Second-order central differencing is used for viscous fluxes. Turbulence is modeled using the Baldwin–Lomax algebraic turbulence model.[17]

The no-slip and impermeable wall conditions were imposed in the present calculations. To focus on off-design flow analyses and simplify the extent of computational parameters, the adiabatic wall is assumed. The outer-boundary conditions were specified as the freestream flow property. The initial flow conditions were specified as uniform freestream flow.

Grid Generation

Because the flowfields to be analyzed and the waverider forebody are symmetrical, half of the waverider forebody is considered. The size of the three-dimensional grid about this half configuration is $51 \times 74 \times 81$ in the streamwise, circumferential, and normal directions, respectively, and it is generated by using a differential equation method.[18] In this grid generation process, some particular rules and criteria[19] are followed. 1) There should be an adequate number of grid points in the laminar sublayer of the turbulent boundary layer to guarantee sufficiently precise skin-friction predictions and to minimize solution sensitivity to grid size. Accordingly, at least four or five grid points are located in the laminar sublayer. 2) Grid lines cannot intersect each other anywhere in the grid domain. This becomes critical in the vicinity of the waverider tips, and some special procedures were implemented involving judicious, but slight, relocation of some grid points in this region. 3) Initially, a two-dimensional grid on the waverider base plane, as shown in Fig. 2, is created by solving the two-dimensional Poisson's equation.[18] Then the entire three-dimensional grid is obtained by extending the two-dimensional grid to the nose of the waverider, using linear interpolation techniques. 4) The grid is finer in the vicinity of the leading edge and nose.

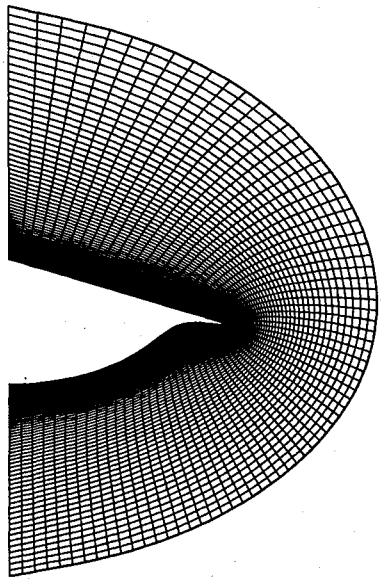

Fig. 2 Two-dimensional grid at the waverider base plane.

Results and Discussion

Before analyzing the complete viscous waverider flowfields, we tested the CFL3D code by simulating some configurations that have known solutions. All results from these test cases show that the code is accurate for the present application and has three-dimensional computational capability.[19]

The main considerations for off-design flowfields about the forebody of the selected conical waverider are presented and discussed. The two off-design cases, turbulent off-design ($\alpha = 5$ deg) and laminar off-design ($M_\infty = 5$), are simulated. In addition, the authors' earlier on-design results are briefly reviewed and used to compare with the off-design simulations.

On-Design Waverider

On-design conditions[4,9] for the chosen waverider are at $M_\infty = 4$ and $\alpha = 0$. The turbulent and laminar waverider flowfields for on-design conditions, $Re = 5.08$ million/foot (M/ft) and $T_\infty = 520°$R, and an adiabatic wall have been simulated.[12,13] Note that the inviscid assumption is inherent to specifying the on-design conditions, inasmuch as the waverider surfaces are designed from stream surfaces in an inviscid supersonic flow. Figures 3 and 4 show simulation results for the pressure-ratio (p/p_∞) contours at the cross plane, $x = 15.67$ in., for the laminar and turbulent cases, respectively. It is clear from these figures that the shocks are not attached precisely to the waverider tips. This detachment is attributed to boundary-layer displacement. However, the conclusion in Refs. 12 and 13 indicated that these slightly detached shocks do not significantly affect the lift and lift-to-drag ratio of the waverider forebody, in comparison with theoretical results[4] and Euler solutions,[11] and the computational pressure coefficients are in agreement with the experimental results.[10] From the cited on-design figures, relatively uniform velocity magnitudes on the waverider lower surface are observed. The flow on the waverider upper surface is basically not disturbed and is thus in agreement with a flat-plate flow. In addition, the oblique shock on the waverider lower surface is quite distinct; thus the shock is well captured by using the CFL3D code.

Figure 5 shows the circumferential variation of the laminar and turbulent on-design local skin-friction coefficients at $x = 15.67$ in.

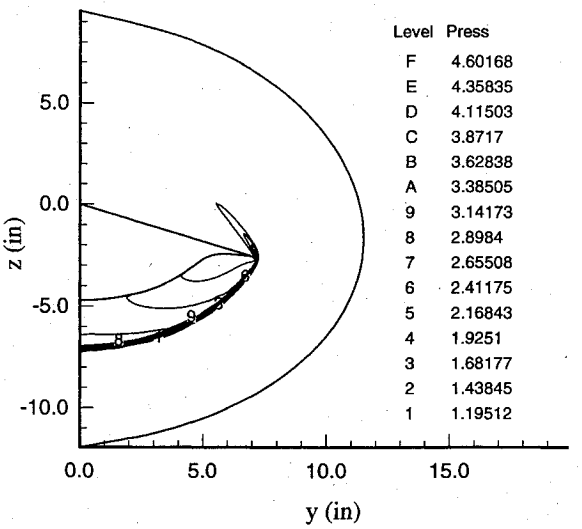

Fig. 3 Two-dimensional pressure-ratio (p/p_∞) contours for the laminar on-design waverider case: x = 15.67 in., M_∞ = 4, Re = 5.08 M/ft, α = 0, adiabatic wall, and T_∞ = 520°R.

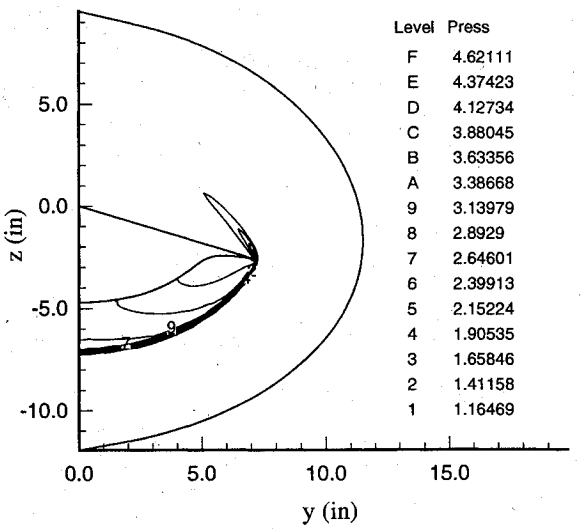

Fig. 4 Two-dimensional pressure-ratio (p/p_∞) contours for the turbulent on-design waverider case: x = 15.67 in., M_∞ = 4, Re = 5.08 M/ft, α = 0, adiabatic wall, and T_∞ = 520°R.

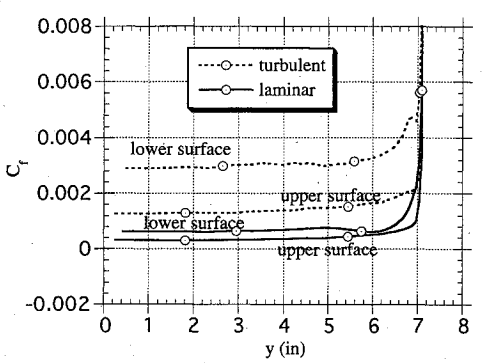

Fig. 5 Circumferential variation of the local skin-friction coefficient for the on-design waverider: x = 15.67 in., M_∞ = 4, Re = 5.08 M/ft, α = 0, adiabatic wall, and T_∞ = 520°R.

Except for the waverider tip region, the local skin-friction coefficient distributions are basically flat. Furthermore, the local skin-friction coefficients on the waverider lower surface are observed to be larger than on the upper surface. The reason for this is that the Mach number M_0 on the lower surface is smaller than on the upper surface because of strong flow compression on the more inclined lower surface. This is analogous to flow past a two-dimensional flat plate with a smaller

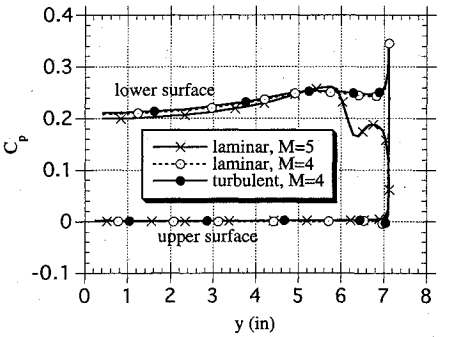

Fig. 6 Circumferential variation of the pressure coefficient for the on-design waverider: x = 15.67 in., Re = 5.08 M/ft, α = 0, adiabatic wall, and T_∞ = 520°R.

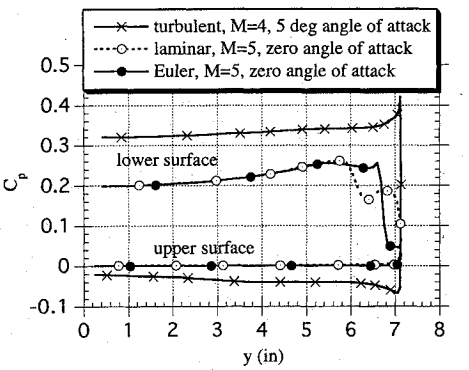

Fig. 7 Circumferential variation of the pressure coefficient for the off-design waverider: x = 15.67 in., Re = 5.08 M/ft, adiabatic wall, and T_∞ = 520°R.

M_0, for which the local skin-friction coefficient is increased with decreasing Mach number.[20] Near the waverider tip, because the characteristic development length for the boundary layer L in the relations

$$C_f \sim \frac{1}{(Re)^n} \quad (n > 0) \qquad \text{and} \qquad Re = \frac{\rho_0 U_0 L}{\mu} \tag{2}$$

is relatively small and becomes smaller with increasing y, the local skin-friction coefficients ultimately are increased, as observed. The expected result that the local skin-friction coefficients for the turbulent case have much larger values than for the laminar case is also observed. Finally, as shown in Fig. 6, the pressure coefficient values for both cases are essentially the same, inasmuch as the viscous effects that cause a thin boundary-layer development (laminar or turbulent) near a surface have minor impact upon surface pressure distribution.

Off-Design Waverider

A flight vehicle cannot always stay on its on-design condition. Thus knowledge of off-design waverider flowfield is very important. For off-design conditions, the authors have considered two cases. One is for laminar flow at M_∞ = 5, Re = 5.08 M/ft, and α = 0 and an adiabatic wall, whereas the other is for turbulent flow at M_∞ = 4, Re = 5.08 M/ft, and α = 5 deg and an adiabatic wall. Additionally, the results from a Euler (inviscid) solution at M_∞ = 5 and α = 0 are included to provide some interesting comparison.

Laminar Waverider

For the laminar flow case at the off-design Mach number, representative simulation results are shown in Figs. 7–13. Figure 7 shows the circumferential variation of the laminar off-design pressure coefficient at x = 15.67 in. Also included are Euler (M_∞ = 5) and turbulent off-design results for comparison purposes. The values of the laminar off-design pressure coefficient on both the upper and lower surfaces in the interior-regions are quite similar to those for the counterpart Euler case, as well as the inviscid cases reported in Ref. 11. Additionally, the laminar off-design trends are consistent with our Euler solution and Ref. 11 in the vicinity of the lower surface tip, with departures in the actual values being attributable

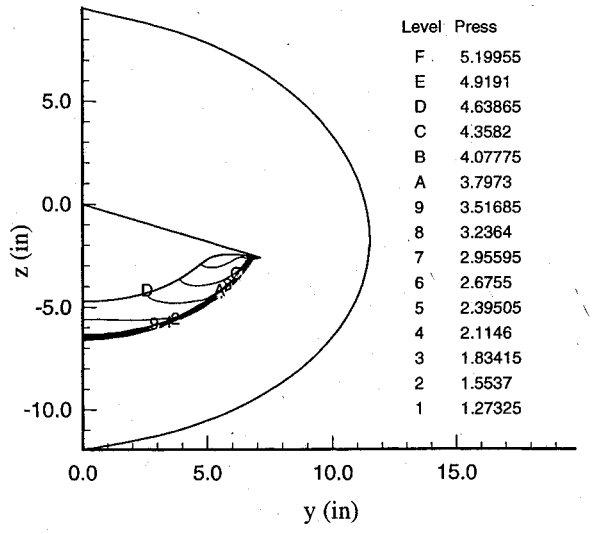

Fig. 8 Two-dimensional pressure-ratio (p/p_∞) contours for the Euler waverider case: x = 15.67 in., M_∞ = 5, Re = 5.08 M/ft, α = 0, adiabatic wall, and T_∞ = 520°R.

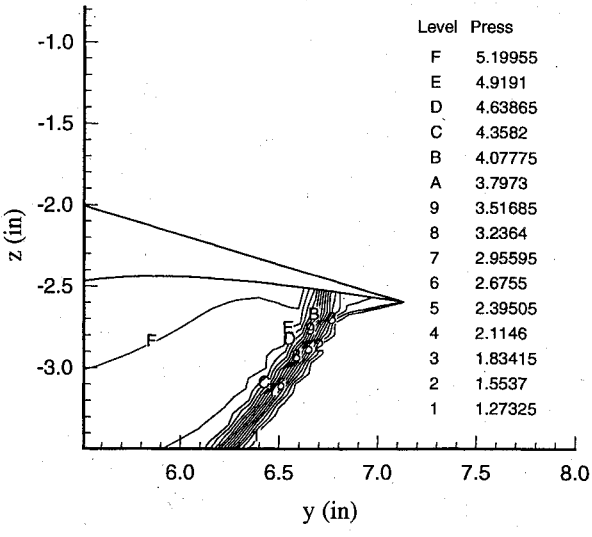

Fig. 9 Two-dimensional pressure-ratio (p/p_∞) contours near the tip for the Euler case: x = 15.67 in., M_∞ = 5, Re = 5.08 M/ft, α = 0, adiabatic wall, and T_∞ = 520°R.

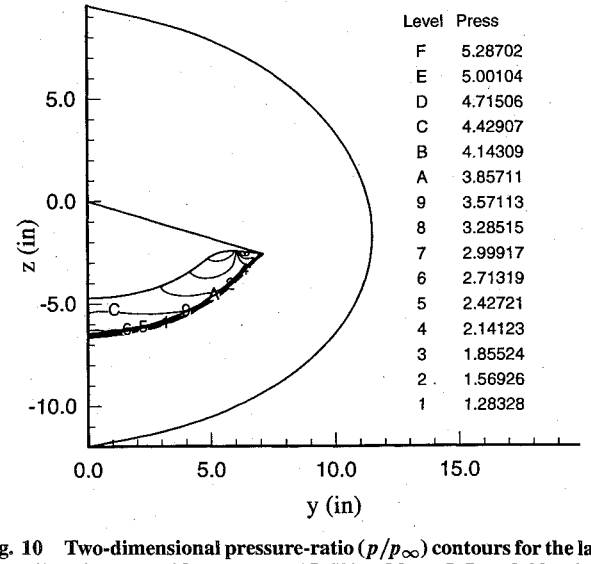

Fig. 10 Two-dimensional pressure-ratio (p/p_∞) contours for the laminar off-design waverider case: x = 15.67 in., M_∞ = 5, Re = 5.08 M/ft, α = 0, adiabatic wall, and T_∞ = 520°R.

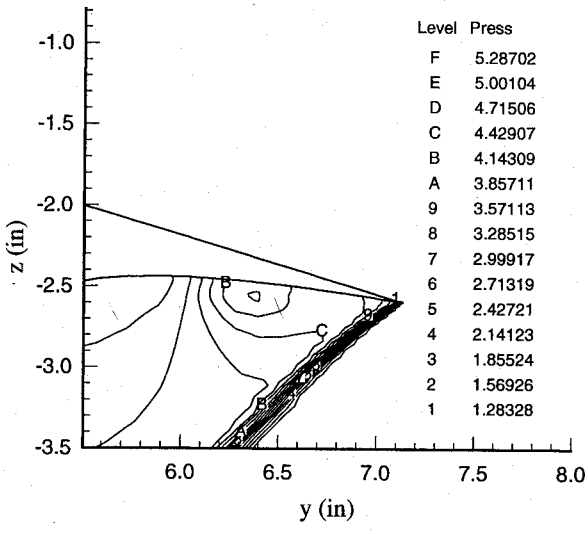

Fig. 11 Two-dimensional pressure-ratio (p/p_∞) contours near the tip for the laminar off-design waverider case: x = 15.67 in., M_∞ = 5, Re = 5.08 M/ft, α = 0, adiabatic wall, and T_∞ = 520°R.

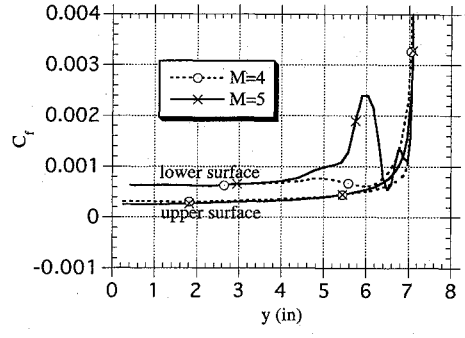

Fig. 12 Circumferential variation of the location skin-friction coefficient for the laminar waverider: x = 15.67 in., Re = 5.08 M/ft, α = 0, adiabatic wall, and T_∞ = 520°R.

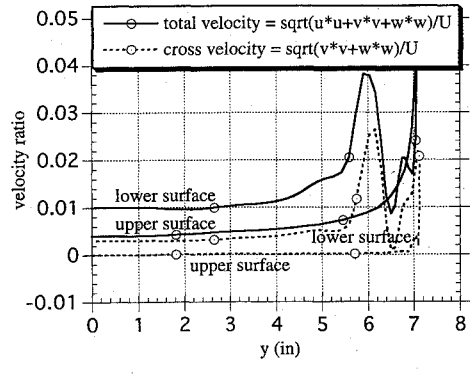

Fig. 13 Circumferential distribution of velocity at the first grid cell centers for the laminar off-design waverider case.

to shock-wave/boundary-layer interactions. In a relatively large region near the centerline on the waverider lower surface, the laminar off-design pressure coefficient is slightly less than the laminar on-design value, as shown in Fig. 6. From the respective areas enclosed by the pressure coefficients on the upper and lower surfaces for the laminar on-design and off-design cases, the laminar on-design lift coefficient is somewhat larger than the laminar off-design lift coefficient. In fact, C_L = 0.7675 and C_D = 0.2325 for the laminar on-design case; C_L = 0.7105 and C_D = 0.2232 for the laminar off-design case.

Figures 8 and 9 show the cross plane pressure-ratio (p/p_∞) contours for the Euler case at the off-design Mach number at x = 15.67 in. It is obvious that the main shock for the waverider is attached on the lower surface rather than at the waverider tip. Additionally, the tip that is outboard of the main shock generates a weak oblique shock, just as a small angle wedge does. Both the main

shock and the oblique shock can cause pressure jumps, as shown in Fig. 7, with the main shock causing a higher pressure jump.

Figures 10 and 11 show the pressure-ratio (p/p_∞) contours for the laminar off-design case at $x = 15.67$ in. It is apparent that the main shock is essentially attached at the waverider tip. Although no shock is attached on the lower surface, there is a significant pressure gradient around $y = 6$–7 in. on the lower surface. It seems that the main shock and the weak oblique shock observed in Fig. 9 for the Euler solution are combined together for the laminar off-design case and form the attached main shock. Obviously, viscous effects result in these changes as herein explained. The fluid viscosity causes a boundary layer near the lower surface, thus reducing the local velocity. Therefore, the pressure jump occurring at about $y = 6.5$ in. resulting from the main shock of the Euler solution, as shown in Figs. 7 and 9, will be allowed to dissipate through this low velocity boundary layer and the pressure disturbance will propagate in the cross plane direction. The propagation in the region of $y < 6.5$ in. results in the pressure gradient around $y = 6$–6.5 in., as shown in Fig. 11. The propagation in the region of $y > 6.5$ in. results in the pressure gradient around $y = 6.5$–7 in. and strengthens the shock at the tip as shown in Fig. 11. In addition, the boundary-layer displacement can also result in the main shock moving to the tip. Thus the shock-wave/boundary-layer interaction and viscous effects at the waverider tip comprehensively affect the pressure coefficient distribution around the waverider tip, as shown in Fig. 7. The main attached shock causes a high pressure jump at the tip.

Figure 12 shows the laminar off-design circumferential variation of the local skin-friction coefficient at $x = 15.67$ in., together with the laminar on-design results. Because of having the same Reynolds number value, the local skin-friction coefficients for both laminar on-design and off-design cases are almost the same in the relatively large region near the center of the waverider. However, because of the differing effects on the main shock and shock-wave/boundary-layer interaction, the off-design local skin-friction coefficient on the lower surface changes rapidly near the tip, in comparison to the on-design case. This situation results from significant cross-flow on the lower surface, driven by a strong pressure gradient, as shown in Fig. 13, which shows the velocity distribution (both cross velocity and total velocity) in the first grid cell centers off the waverider surface. The first cell velocity distribution and the local skin-friction coefficient have exactly the same trends as seen by comparing Figs. 12 and 13. Furthermore, these parameters show basically the same trend as the pressure coefficient in Fig. 7. Obviously, the crossflows, shown in Fig. 13, are driven by the pressure gradients depicted in Fig. 7.

Turbulent Waverider

For the turbulent flow case at the off-design angle of attack, simulation results are shown in Figs. 14–18, as well as the previously cited Fig. 7. Figures 14 and 15 show the pressure-ratio (p/p_∞) contours and Mach number contours, respectively, at $x = 15.67$ in. These figures reveal that the main oblique shock at the waverider tip region is apparently detached for this case. The shock is well captured. In addition, from Fig. 15, there is observed to be a velocity gradient normal to the surface in a relatively large region near the centerline region on the upper surface. This phenomenon results from a vortex existing in that region, as shown by the crossflow velocity vectors and streamlines in Fig. 16. Obviously, from considering Fig. 16, there is a strong vortex on the upper surface near the centerline. In addition, there appears a small separation bubble near the tip on the upper surface. This feature becomes more clear from a blowup plot near the tip presented in Fig. 17. Because of this vortex and the small bubble, the pressure coefficient on the upper surface changes subtly at corresponding locations, as can be observed in Fig. 7.

Referring back to Fig. 7, we consider the turbulent off-design pressure coefficient. Compared with the other cases in Fig. 7, the turbulent off-design pressure coefficient on the upper surface has the lowest values, because the flow on the upper surface at 5-deg angle of attack is expanded after crossing the expansion waves emanating from the waverider leading edge. On the contrary, the turbulent off-design pressure coefficient on the lower surface is the highest one, since the flow on the lower surface at 5-deg angle of attack

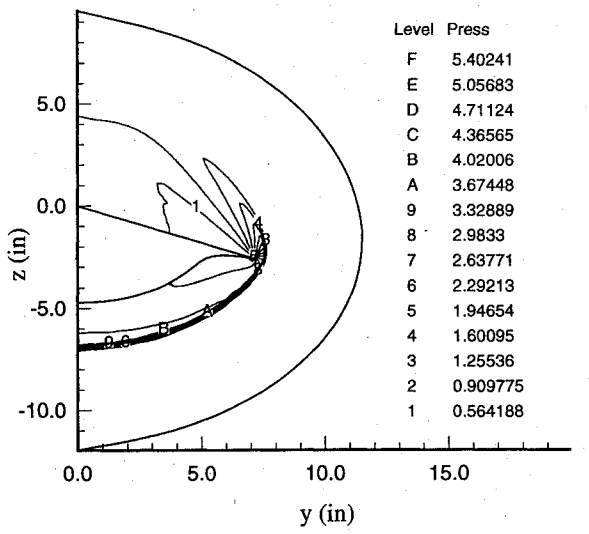

Fig. 14 Two-dimensional pressure-ratio (p/p_∞) contours for the turbulent off-design waverider case: $x = 15.67$ in., $M_\infty = 5$, $Re = 5.08$ M/ft, $\alpha = 5$ deg, adiabatic wall, and $T_\infty = 520°$R.

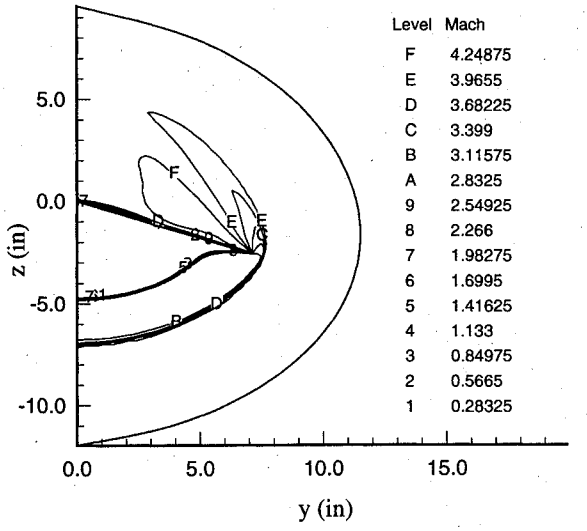

Fig. 15 Two-dimensional Mach number contours for the turbulent off-design waverider case: $x = 15.67$ in., $M_\infty = 4$, $Re = 5.08$ M/ft, $\alpha = 5$ deg, adiabatic wall, and $T_\infty = 520°$R.

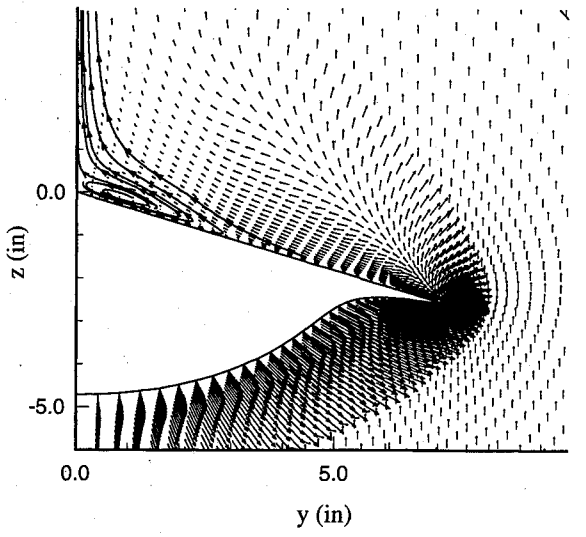

Fig. 16 Crossflow velocity vectors and selected streamlines for the turbulent off-design waverider case: $x = 15.67$ in., $M_\infty = 4$, $Re = 5.08$ M/ft, $\alpha = 5$ deg, adiabatic wall, and $T_\infty = 520°$R.

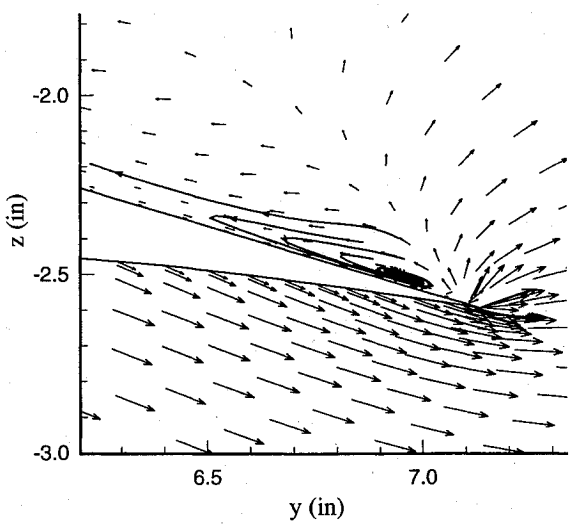

Fig. 17 Crossflow velocity vectors and selected streamlines near the tip for the turbulent off-design waverider case: x = 15.67 in., M_∞ = 4, Re = 5.08 M/ft, α = 5 deg, adiabatic wall, and T_∞ = 520°R.

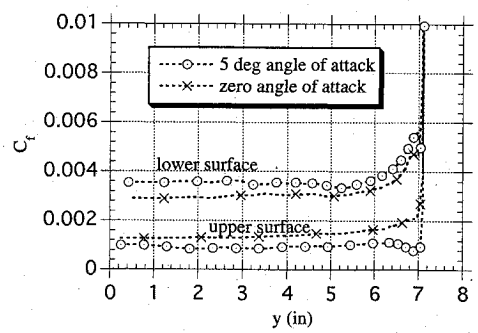

Fig. 18 Circumferential variation of the location skin-friction coefficient for the turbulent waverider: x = 15.67 in., Re = 5.08 M/ft, M_∞ = 4, adiabatic wall, and T_∞ = 520°R.

receives greater compression by the main shock wave. Thus, the turbulent off-design case has the highest lift coefficient among those cases investigated (Fig. 7).

The circumferential variation of local skin-friction coefficient at $x = 15.67$ in. is shown in Fig. 18. Because there is a larger M_0 caused by expansion waves on the waverider upper surface for the off-design case, the local skin-friction coefficient is smaller than for the turbulent on-design case. The reasoning is similar to that discussed in the preceding section, "On-Design Waverider." On the contrary and for a similar reason, the local skin-friction coefficient on the lower surface for the off-design case is larger. For this turbulent off-design case, the small separation bubble near the tip of the upper surface results in a significant variation of the local skin-friction coefficient with respect to the on-design counterpart, whereas the major vortex near the centerline results in only a slight variation in the C_f distribution.

Conclusions

All results for the selected waverider forebody configuration are reasonable and can be physically explained. For on-design cases, the main oblique shock is well captured. The flowfield on the waverider lower surface around the centerline is relatively uniform. The viscous effects do not basically affect surface pressure distribution. However, there is a strong shock-wave/boundary-layer interaction at the waverider tip. This results in the shock being detached at the tip.

For the laminar off-design case ($M_\infty = 5$), the main oblique shock is attached. The values of the laminar off-design pressure coefficient and local skin-friction coefficient on both upper and lower surfaces in the interior regions are quite similar to those for the counterpart laminar on-design case. But in the vicinity of the lower surface tip, the departures in the actual values are obvious because of shock-wave/boundary-layer interactions.

For the turbulent off-design ($\alpha = 5$ deg), the main oblique shock is detached. The values of the turbulent off-design pressure coefficient and local skin-friction coefficient on both upper and lower surfaces are quite different from those for the counterpart turbulent on-design case. In the vicinity of the upper surface tip, there is a small separation bubble. And in the interior region on the upper surface, there is a strong vortex.

All revealed phenomena are very important to understanding the flowfields for both on-design and off-design conditions. The results are useful under some circumstances for the consideration of scramjet design, aerodynamic heating, separated flow, vehicle handling and control, vehicle stability, and afterbody design.

Acknowledgments

The authors thank the National Center for Supercomputer Applications, University of Illinois, for a grant for the use of the Cray Y-MP computer, on which the CFL3D code has been run. The authors also thank Jim Thomas, NASA Langley Research Center, for making the CFL3D code available. The grid system has been generated by extending the grid generation procedure used in GRAPE, a computer program written at the NASA Ames Research Center.

References

[1]Nonweiler, T. R. F., "Aerodynamic Problems of Manned Space Vehicles," *Journal of the Royal Aeronautics Society*, Vol. 63, No. 585, 1959, pp. 521–528.

[2]Nardo, C. T., "Aerodynamic Characteristics of Two-Dimensional Waverider Configurations," *AIAA Journal*, Vol. 10, No. 9, 1972, pp. 1258–1261.

[3]Jischke, M. C., "Supersonic Flow Past Conical Bodies with Nearly Circular Cross Sections," AIAA Paper 80-0028, Jan. 1980.

[4]Rasmussen, M. L., "Waverider Configurations Derived from Inclined Circular and Elliptic Cones," *Journal of Spacecraft and Rockets*, Vol. 17, No. 6, 1980, pp. 537–545.

[5]Bowcutt, K. G., Anderson, J. D., and Capriotti, D., "Viscous Optimized Hypersonic Waveriders," AIAA Paper 87-0272, Jan. 1987.

[6]Corda, S., and Anderson, J. D., Jr., "Viscous Optimized Hypersonic Waveriders Designed from Axisymmetric Flow Fields," AIAA Paper 88-0369, Jan. 1988.

[7]Hemdan, H. T., and Jischke, M. C., "Inlets for Waveriders Derived from Elliptic-Cone Stream Surfaces," *Journal of Spacecraft and Rockets*, Vol. 24, No. 1, 1987, pp. 23–32.

[8]O'Neill, M. K. L., and Lewis, M. J., "Optimized Scramjet Integration on a Waverider," *Journal of Aircraft*, Vol. 29, No. 6, 1992, pp. 1114–1121.

[9]Rasmussen, M. L., Jischke, M. C., and Daniel, D. C., "Experimental Forces and Moments on Cone-Derived Waveriders for M = 3 to 5," AIAA Paper 81-0149, Jan. 1981.

[10]Jischke, M. C., Rasmussen, M. L., and Daniel, D. C., "Experimental Surface Pressures on Cone-Derived Waveriders for M = 3–5," *Journal of Spacecraft and Rockets*, Vol. 20, No. 6, 1983, pp. 539–545.

[11]Yoon, B. H., and Rasmussen, M. L., "Computational Analysis of Hypersonic Flows Past Elliptic-Cone Waveriders," Dept. of Aeronautical and Mechanical Engineering, Univ. of Oklahoma, Research Rept. OU-AME-91-2, Norman, OK, Jan. 1991.

[12]Liao, J. R., Isaac, K. M., Miles, J. B., and Tsai, B. J., "Navier–Stokes Simulation for Cone-Derived Waverider," *AIAA Journal*, Vol. 30, No. 6, 1992, pp. 1521–1528.

[13]Tsai, B. J., Miles, J. B., and Isaac, K. M., "Computation of Turbulent Flow About Cone-Derived Waverider," AIAA Paper 92-2726, June 1992.

[14]Takashima, N., and Lewis, M. J., "Navier–Stokes Computation of a Viscous-Optimized Waverider," AIAA Paper 92-0305, Jan. 1992.

[15]Anderson, D. A., Tannehill, J. C., and Pletcher, R. H., "Computational Fluid Mechanics and Heat Transfer," 1st ed., Hemisphere, New York, 1984, pp. 190–197, 421–424.

[16]Roe, P. L., "Approximate Riemann Solvers, Parameter Vectors and Difference Schemes," *Journal of Computational Physics*, Vol. 43, No. 2, 1981, pp. 357–372.

[17]Baldwin, B. S., and Lomax, H., "Thin Layer Approximation and Algebraic Model for Separated Turbulent Flows," AIAA Paper 78-257, Jan. 1978.

[18]Sorenson, R. L., "A Computer Program to Generate Two-Dimensional Grids About Airfoils and Other Shapes by the Use of Poisson's Equation," NASA TM 81198, May 1980.

[19]Shi, Y., "Off-Design Waverider Flowfield CFD Simulation," Ph.D. Dissertation, Dept. of Mechanical and Aerospace Engineering, Univ. of Missouri, Columbia, MO, 1995.

[20]Schlichting, H., "Boundary-Layer Theory," 7th ed., McGraw–Hill, New York, 1987, pp. 717–720.

K. J. Weilmuenster
Associate Editor